frontiers in Materials

ORIGINAL RESEARCH
published: 11 December 2019
doi: 10.3389/fmats.2019.00317

Effect of Yttrium Contents on the Microstructure of a Hot-Rolled Tantalum-Containing 12Cr-ODS Steel

Changhao Wang[1,2], *Jinru Luo*[1]*, *Ning Guo*[3]*, *Jian Tu*[2], *Hong Ye*[2], *Pengcheng Zhang*[1] and *Qingzhi Yan*[4]

[1] Institute of Materials, China Academy of Engineering Physics, Mianyang, China, [2] School of Material Science and Engineering, Chongqing University of Technology, Chongqing, China, [3] School of Materials and Energy, Southwest University, Chongqing, China, [4] School of Material Science and Engineering, University of Sciences and Technology Beijing, Beijing, China

Dual-phase oxide dispersion strengthened (ODS) steels of Fe−12Cr–*x*Y (x = 0.1, 0.2, and 0.3 wt%) have been fabricated by casting, hot-forging and subsequent hot-rolling. Microstructure of the hot-rolled samples was carefully characterized by use of electron probe microanalysis (EPMA), electron backscatter diffraction (EBSD), and transmission electron microscope (TEM). The results show that all the samples consist of ferrite phase with coarse fiber grains (elongated along the rolling direction) and martensite phase in the form of fine block grains. As the Y addition increases, the ratio of ferrite to martensite and density of low-angle boundaries (LABs) within the martensite and ferrite grains do not change significantly. The Y_2O_3 particles introduced by self-oxidation during casting are survived without being dissolved or refined after hot-forging and hot-rolling. However, as the Y addition increases, the Y_2O_3 particles tend to aggregate with fine $M_{23}C_6$ and TaC carbides. The hardness of the sample with high Y additions is lower than that of the samples with none or low Y additions, which could be attributed to the aggregation coarsening of the yttria and TaC particles, resulting in a decrease in dispersion strengthening effect. The effect of Y additions on microtexture was also discussed.

Keywords: ODS steel, yttrium, hot-rolling, microstructure, tantalum

OPEN ACCESS

Edited by:
Yanzhong Tian,
Northeastern University, China

Reviewed by:
Hai-Tao Liu,
Northeastern University, China
Lijia Zhao,
ArcelorMittal USA LLC, United States

***Correspondence:**
Jinru Luo
ada669@qq.com
Ning Guo
guoning_1000@163.com

Specialty section:
This article was submitted to Structural Materials, a section of the journal Frontiers in Materials

Received: *14 October 2019*
Accepted: *21 November 2019*
Published: *11 December 2019*

Citation:
Wang C, Luo J, Guo N, Tu J, Ye H, Zhang P and Yan Q (2019) Effect of Yttrium Contents on the Microstructure of a Hot-Rolled Tantalum-Containing 12Cr-ODS Steel. Front. Mater. 6:317. doi: 10.3389/fmats.2019.00317

BACKGROUND

Nuclear energy is considered to be one of the clean and efficient energy sources and plays a significant role in addition to natural renewable energy sources (Saito, 2010). The further development of nuclear energy is an important way for mankind to solve the future energy crisis. In this regard, the development and application of the Generation-IV (Gen-IV) nuclear reactors are on the horizon (Abram and Ion, 2008; Locatelli et al., 2013). The structural materials used in the Gen-IV reactors need to endure much higher temperatures, more neutron doses, and extremely corrosive environment. Therefore, the development of high-performance and reliability structural materials is the primary consideration for the successful deployment of the Gen-IV reactor systems (Murty and Charit, 2008).

Oxide dispersion strengthened (ODS) steels have been considered as one of the most promising candidate materials due to their many advantages at high-temperature, such as low thermal

expansion, good thermal conductivity, excellent mechanical strength and structural stability, good corrosion resistance, and radiation resistance (Klueh et al., 2005; Murty and Charit, 2008; Corpace et al., 2017; Xu et al., 2019). Generally, ODS steels can be considered as a metal matrix composite composed of steel matrix and nano-scale oxides distributed in the matrix. So far, there are mainly three candidate ODS steels for the fuel cladding materials, which can be classified into austenitic group (Wang et al., 2013), ferritic group (Ren et al., 2018), and ferritic/martensitic dual-phase group (Klueh et al., 2002a) according to their crystal structures of the matrix. Generally, the austenitic ODS steels have better corrosion resistance/oxidation resistance (Wang et al., 2013), while the ferrite ODS steels have higher creep resistance at elevated temperature (Klueh et al., 2002b). The ferritic/martensitic dual-phase ODS steels have superior swelling resistance and excellent thermal properties compared to the austenitic ODS steels (Klueh et al., 2002a). The internal nano-scale oxide particles can provide a high density of pinning sites for grain boundaries and dislocations, and also give huge particle-matrix interfaces as the effective sinks to capture the nuclear transmutation products (Lu et al., 2013), thereby further improving the high-temperature performance of the ODS steels.

Traditionally, the ODS steels are fabricated by mechanical alloying (MA) combined with powder metallurgy sintering followed by hot deformation consolidation (Zhao et al., 2018a). However, in recent years, many studies have found that this method has some disadvantages in the preparation of the Y_2O_3-containing ODS steels. For example, Kimura et al. (1999) reported that Y_2O_3 particles are not only fragmented, but also decomposed during the MA processing. Subsequently, many researchers (Larson et al., 2001; Ukai and Fujiwara, 2002; Miller et al., 2003; Zeybek et al., 2014) found that the added Y_2O_3 can react with Ti, Si, O, etc. in the steel matrix during the MA processing, and the actual dispersion distribution particles are composite oxide clusters/particles, such as Y-Cr-O ($YCrO_3$), Y-Ti-O ($Y_2Ti_2O_3$, Y_2TiO_5, $Y_2Ti_2O_7$, etc.), and Y-Si-O (Y_2Si_2O), rather than Y_2O_3. Since the thermal stability of the composite oxide clusters/particles is not as good as that of the Y_2O_3 particles, resulting in the degradation of the high-temperature performance and the neutron radiation resistance (Zeybek et al., 2014). Therefore, it is worthy to develop new methods for preparing Y_2O_3-containing ODS steels, which can avoid the reaction of Y_2O_3 particles and steel matrix. In this study, a ferritic/martensitic dual-phase ODS steel was fabricated by casting followed by hot-forging and hot-rolling. The Y_2O_3 was induced by self-oxidation of the pure yttrium addition during the stirring casting. Microstructure of the hot-rolled samples was carefully characterized and analyzed. The effect of Y additions on microtexture and microhardness was also studied.

EXPERIMENTAL TECHNIQUE

A 12Cr steel with the chemical composition of Fe-12.0%Cr-1.0%Mo-1.1%W-1.0%Mn-0.2%V-0.15%Ta-0.03%Ti-0.07%N-0.15%Si (wt%) was designed as the steel matrix. The steel was re-melted and poured into a mold pre-plated with pure yttrium powders (with 99.9% purity), and then solidified rapidly from 1,600°C to room temperature under the protective argon atmosphere. Four ingots (about 100 KG each) with different contents of yttrium (0, 0.1, 0.2, and 0.3 wt%) were prepared. The ingots were hot-forged into sticks with a dimension of 240 mm × 240 mm at ∼900°C, and finally hot-rolled (at ∼900°C, with the rolling direction (RD) perpendicular to the forging direction) into plates with 30 mm thickness followed by water cooling. The total reduction rate is about 87.5%. The entire preparation process is described in detail in Chen et al. (2019). The four samples are denoted as 12Cr-0Y, 12Cr-0.1Y, 12Cr-0.2Y, and 12Cr-0.3Y, respectively.

Specimens were cut from the rolled sheets. The RD-ND (normal direction) sections were selected and characterized. An electron probe microanalysis (EPMA, EPMA-1720H, SHIMADZU, Kyoto, Japan) was used to quantitatively analyze the composition of the second phase particles. Optical microscope (OM, DMI5000 M, Leica, Leica Instruments GmbH, Germany) and field emission gun scanning electron microscope (FEG-SEM, Zeiss Sigma HD, Zeiss, Dresden, Germany) equipped with backscattered electron imaging (BSEI) and electron backscattered diffraction (EBSD, AZtech Max2, Oxford Instruments, London, UK) were used to characterize the microstructure. A field emission gun transmission electron microscope (FEG-TEM, Tecnal G2 F20, FEI Company, Hillsboro, OR, USA) equipped with energy dispersive spectrometry (EDS, Oxford Instruments, London, UK) was applied to characterize the microstructure and elemental distribution. Prior to OM/EPMA/BSEI/EBSD, samples were ground and electropolished in an electrolyte of 10% perchloric acid and 90% methanol at −20°C. The OM samples were etched by a mixed solution consisting of 10 ml nitric acid, 1 ml hydrofluoric acid, and 50 ml deionized water. The TEM samples were ground and then thinned by twin-jet electropolishing (MTP-1A, Yulong Co., Ltd., Beijing, China). The electrolyte was 10% perchloric acid and 90% methanol, and the polishing temperature was about −30°C.

RESULTS AND DISCUSSION

Scenario 1: Dual-Phase Structure and Texture

It is well-known that the 12Cr ODS is a typical ferritic-martensitic dual-phase steel (Chen et al., 2015, 2019; Yao et al., 2018). **Figure 1** shows the optical microstructure of the 12Cr ODS steel with different Y additions. As can be seen, a dual-phase structure composed of alternating fibrous grained ferrite (α-Fe, bright fiber regions) and martensite (α'-Fe, dark block regions) can be clearly identified. The ferrite grains are elongated in the RD to present the fibrous structure. It has been reported that the addition of alloys such as Al (Xu et al., 2019), Ti (Zhao et al., 2018b) can reduce the martensite lath in the ferritic/martensitic dual-phase ODS steels, and even obtain single-phase ferrite ODS steel. The relative ferrite content (area fraction) plotted as a function of the Y content is displayed in **Figure 2**. For each sample, more than 10 OM images were employed to determine

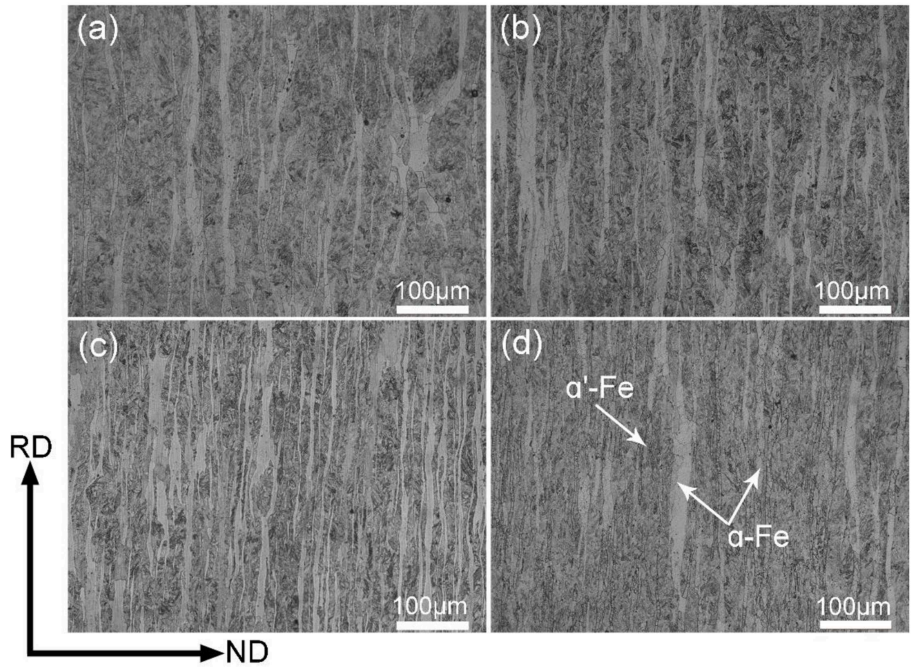

FIGURE 1 | Optical micrographs showing microstructure of various samples along the RD-ND plane: **(a)** 12Cr-0Y, **(b)** 12Cr-0.1Y, **(c)** 12Cr-0.2Y, **(d)** 12Cr-0.3Y.

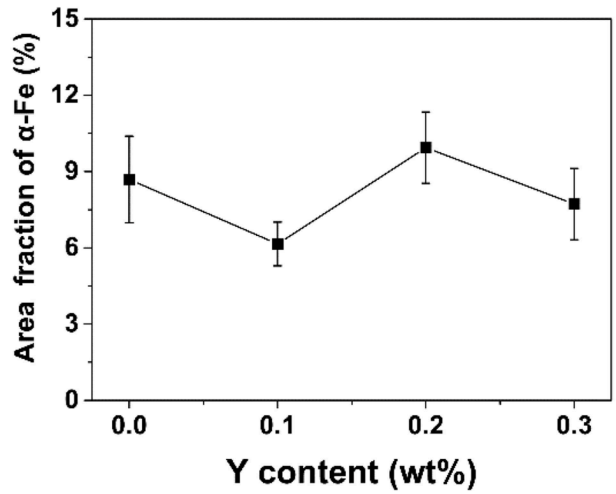

FIGURE 2 | Area fraction of α-Fe plotted as a function of Y contents.

the ferrite content. It indicates that as the Y content increases, the ferrite content does not vary significantly.

The BSEI images confirm the dual-phase structure, as shown in **Figures 3a–d**. High magnification images show that the fibrous grains of α-Fe are composed of a large number of subgrains. These subgrains have an equiaxed shape and an average size of about 2.6 μm in diameter. It has been reported that the subgrains are generated via dislocation climbing and sliding during hot-deformation, and the formation of subgrains is indicative of continuous dynamic recrystallization (CDRX) (Zhao et al., 2018a). The block α'-Fe grains consist of a large number of laths (see arrows in **Figures 3A–D**) which are typical morphologies of martensite with low-carbon contents. It has been reported that for the dual-phase ODS steels fabricated by MA, the second phase particles are often distributed in the ferrite grains rather than in martensite regions (Xu et al., 2019). However, in this study, the second phase particles are observed in both the ferrite and martensite grains, as shown in **Figures 3B,C**.

Figure 4 shows the EBSD results of various samples with different Y additions. The inverse pole figure (IPF) coloring maps and {110} pole figures of α-Fe and α′-Fe are drawn from the EBSD data. The grain boundary (GB) and Kernel average misorientation (KAM) maps of various samples are shown in **Figure 5**. The high-angle boundaries (HABs) and low-angle boundaries (LABs) are highlighted in black and red, respectively, in the GB maps. As can be seen, the fiber grains of α-Fe and martensite laths can be clearly distinguished from the EBSD results. It confirms that the grain size of the a-Fe is much larger than that of the α'-Fe. Moreover, there are more LABs in the α'-Fe corresponding to dislocation martensite with a low-carbon content compared to the fiber α-Fe grains. In the austenitic-martensitic dual-phase steels, it is also found that the amount of LABs in the martensite phase is greater than in the austenite phase (Guo et al., 2018; Zhang et al., 2019).

The KAM values are considered to be related to local misorientation (dislocation density) inside grains (Calcagnotto et al., 2010; Guo et al., 2017), and usually KAM $> 1°$ is considered to be a deformed form, and $<1°$ is a recrystallized state (Lin et al., 2014). As shown in **Figure 5A**, obviously, the fibrous ferrite has a

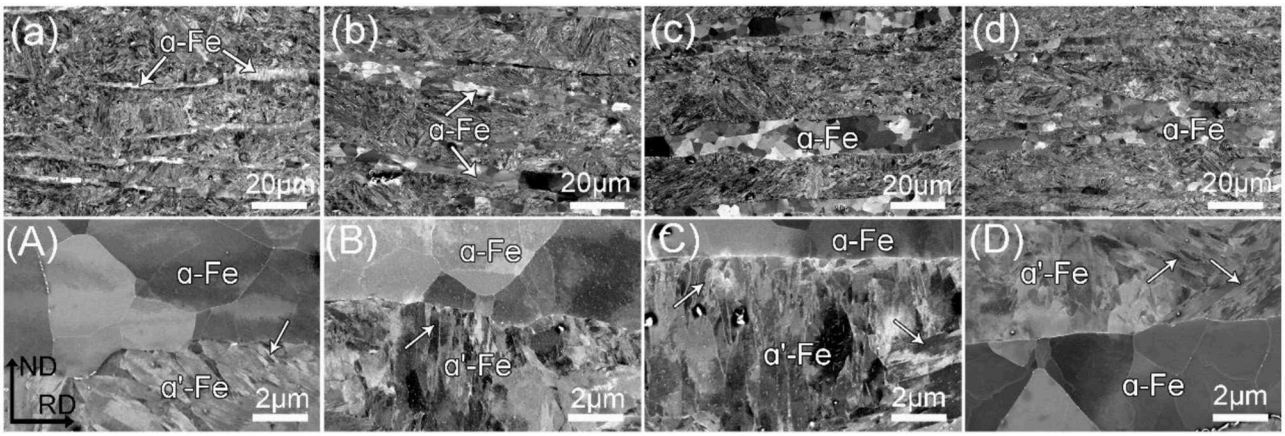

FIGURE 3 | BSEI images of various samples with different Y contents: **(a)** 12Cr-0Y, **(b)** 12Cr-0.1Y, **(c)** 12Cr-0.2Y, **(d)** 12Cr-0.3Y. The figures **(A–D)** are high magnification images of the figures **(a–d)**, respectively.

lower KAM value (<1°) than the martensite, corresponding to a lower dislocation density. **Figure 6** shows the TEM bright field image of the 12Cr-0.3Y sample. It also confirms that the fiber ferrite grains are composed of substantially equiaxed subgrains containing very few dislocations. The average KAM value of the martensite region is slightly larger than 1° (about 1.3°), which is a typical characterize of the hot-rolled metals after water quenching. The ferrite grains are deformed during hot-rolling, resulting in the appearance of the fiber microstructure of the ferrite phase. However, the fiber grains undergo recovery and/or recrystallization due to high-temperature hot-rolling, resulting in a decrease in the dislocation density within the fiber grains and a small KAM value. Moreover, since the austenite grains becomes hard martensite during cooling after hot-rolling, the migration of ferrite grain boundaries and equiaxed crystallization are restricted, eventually resulting in the formation of the fiber ferrite grains with a low dislocation density.

The statistical results show that the densities of LABs and HABs do not change significantly with the increase of Y addition, indicating that the relative content of α'-Fe phase and the average grain size of both martensite and ferrite change little. This is because that although the Y contents of the four samples are different, the Y atoms are mainly present in the steel matrix in an oxide rather than a solid solution state, and the difference in the Y content does not affect the size of the austenite phase region, resulting in the similar content of martensite phase in the four samples.

As shown in **Figure 4**, the pole figure shows that the crystal orientation of martensite and ferrite is preferentially aligned after hot-rolling. From **Figure 4A**, a weak α-fiber texture (also known as RD-fiber texture running from {001}<110> to {111}<110>) can be identified in the martensite phase. As the Y addition increases, the characteristic and density of the α-fiber do not change significantly. When the austenite is recrystallized, the transformation products will have a weak texture (Patricia and John, 1996). In addition, due to the coexistence of the softer ferrite phase, the martensite phase undergoes minimal deformation, resulting in a weaker texture. In contrast, for the ferrite phase, the textures vary with increasing Y addition.

Figure 7 shows the orientation distribution function (ODF) sections of the α-Fe phase of various samples. The ideal rolling textures in BCC metals are illustrated in **Figure 7A**. A {001} <110> texture is observed in the 12Cr-0Y sample (see **Figure 7B**), and no typical BCC rolling textures are found in the 12Cr-0.1Y and 12Cr-0.2Y samples (see **Figures 7C,D**). For the 12Cr-0.3Y sample, as shown in **Figure 7E**, only a strong θ-fiber texture running from {001}<110> to {111}<110> can be identified. It has been reported that the θ-fiber is a dominated recrystallization texture in low-carbon steels during warm rolling in the ferrite phase (Kestens et al., 1996). For the rolling texture, it is well-known that the formation and degradation of each texture component is closely related to the rolling reduction, e.g., the γ fiber texture is gradually substituted by one or more components of the {h11}<1/h,1,2> fiber with increasing rolling reduction (Kestens and Pirgazi, 2016). Owing to the lack of samples with different rolling reductions, the formation mechanism of the texture component cannot be revealed in this study. However, it is still considered that the difference in texture of the ferrite phase is related to the difference in contents of Y_2O_3 particles due to that different number and/or size of the oxide particles has different pinning effects on the dislocation ship and grain rotation during rolling deformation. It is because that alloys can affect textures by changing the planarity of dislocation slip or the frequency of shear banding, but the rolling texture of the BCC metals is not considerably affected by solute additions (Kestens and Pirgazi, 2016).

Scenario 2: Morphology and Distribution of Y_2O_3 and Carbides

High magnification BSEI images show that there are many extremely fine particles precipitate at the grain boundaries, as shown in **Figure 8a**. The EDS results show that such particles contain more C, Cr, and Mo (see **Figure 8b**). It has been reported that the $M_{23}C$ carbides tend to precipitate along the martensite

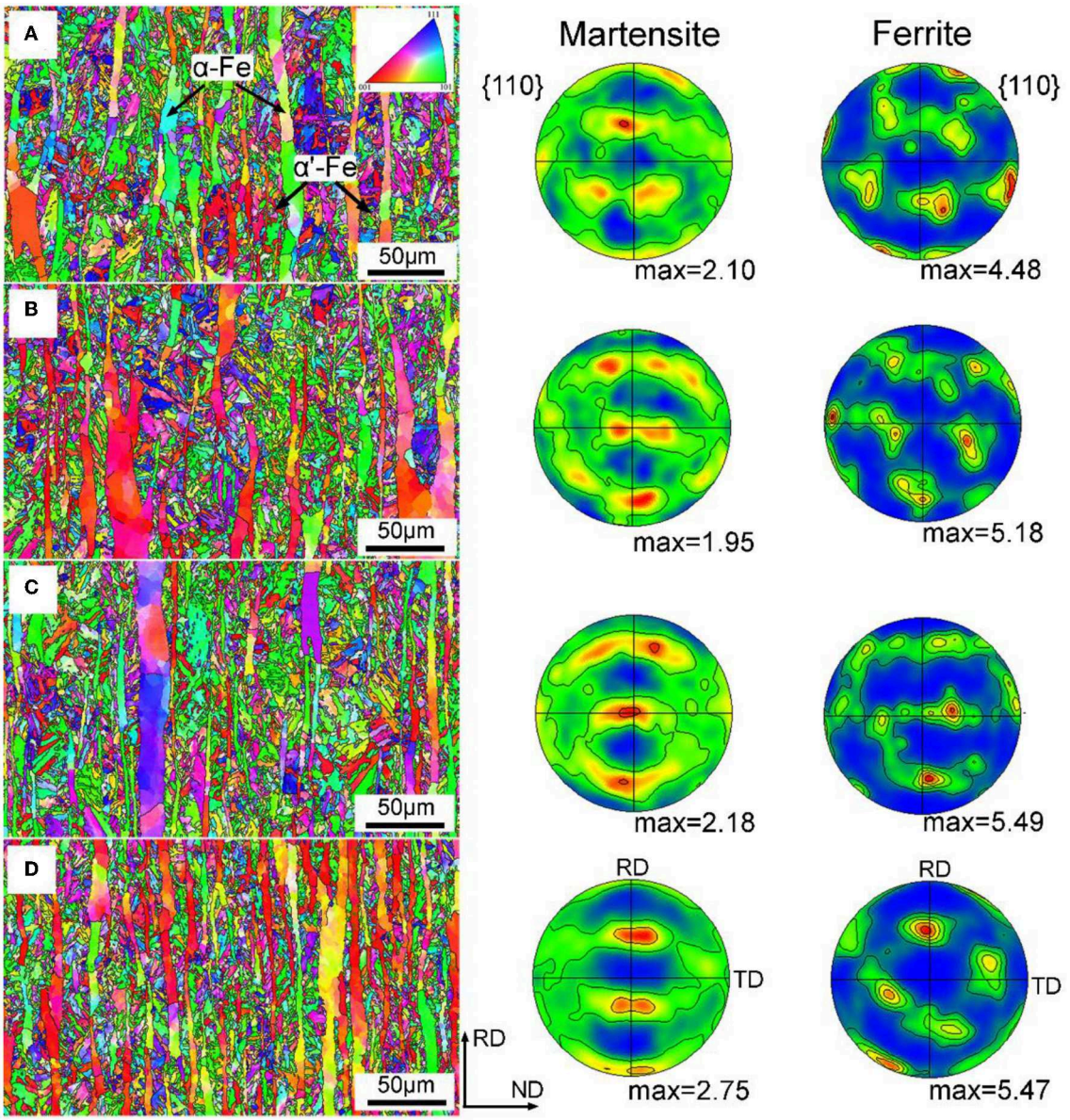

FIGURE 4 | Inverse pole figure (IPF) maps and {110} pole figure of various samples: **(A)** 12Cr-0Y, **(B)** 12Cr-0.1Y, **(C)** 12Cr-0.2Y, **(D)** 12Cr-0.3Y.

laths and grain boundaries in the Y-bearing steel due to the redistribution of carbon between austenite and ferrite resulting from the ferrite favoring element of Y (Chen et al., 2019). The EPMA results show that the micron-sized stripe particles are mainly TaC, as shown in **Figure 9**. The addition of Ta can play two roles: first, Ta as a strong carbide former can inhibit grain growth leading to the improved strength of the ODS steels (Rahmanifard et al., 2015); second, the sufficient Ta available in solid solution can increase the cleavage stress resulting in superior impact properties of the steels (Li et al., 2007). It is well-known that the TaC ceramic particles are one of the main added phases of metal matrix composites due to their high melting point (3880°C), high modulus (540 GPa), high hardness (15–19 GPa), and good chemical stability, etc. (Kim et al., 2009; Khaleghi et al., 2010; Zhou et al., 2017). Compared **Figures 9c,d** to **Figures 9a,b**, it can be seen that as the Y content increases, the TaC particles begin to be enriched in Y.

TEM bright field image and corresponding EDS elemental maps of the 12Cr-0.3Y are shown in **Figure 10**. **Figure 10a** shows typical morphologies of the second phase particles distributing in the in the α'-Fe region. As can be seen, the biggest particle is mainly composed of Y and O (see **Figures 10b,c**), corresponding to Y_2O_3. The diameter of the Y_2O_3 particle is measured as about 800 nm. The Y_2O_3 particle is closely surrounded by fine carbides which mainly consist of C, W and Ta elements (see **Figures 10d–f**). Such carbides have a diameter

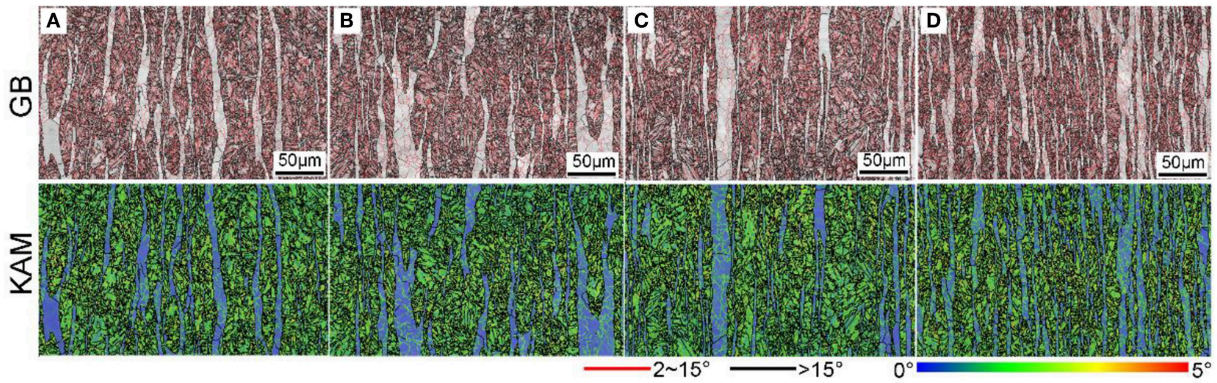

FIGURE 5 | Grain boundary (GB) and Kernel average misorientation (KAM) maps of various samples: **(A)** 12Cr-0Y, **(B)** 12Cr-0.1Y, **(C)** 12Cr-0.2Y, **(D)** 12Cr-0.3Y.

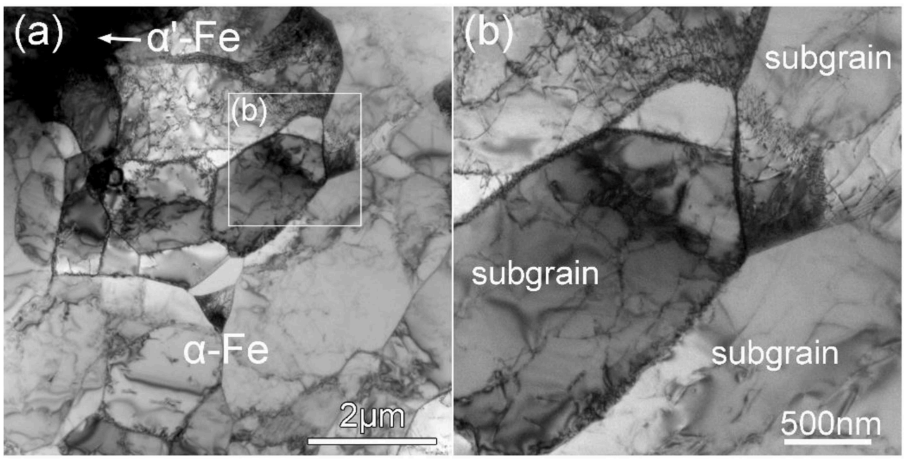

FIGURE 6 | TEM bright field images showing subgrains within α-Fe phase in 12Cr-0.3Y sample: **(a)** low magnification; **(b)** high magnification.

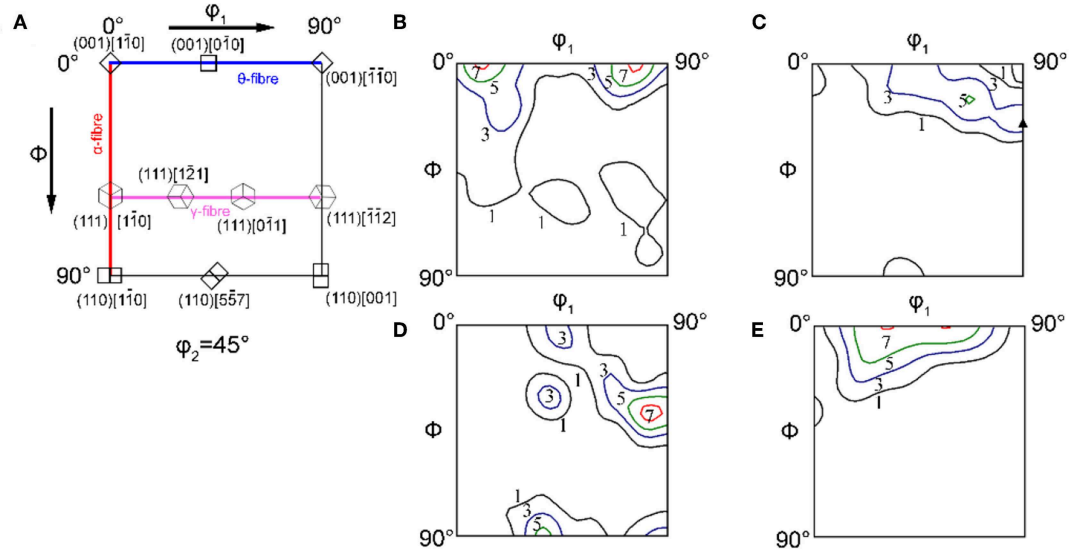

FIGURE 7 | Sections of ODF showing misorientation evolution of α-Fe with increasing yttrium addition: **(A)** ideal rolling textures in BCC metal; **(B)** 12Cr-0Y, **(C)** 12Cr-0.1Y, **(D)** 12Cr-0.2Y, **(E)** 12Cr-0.3Y.

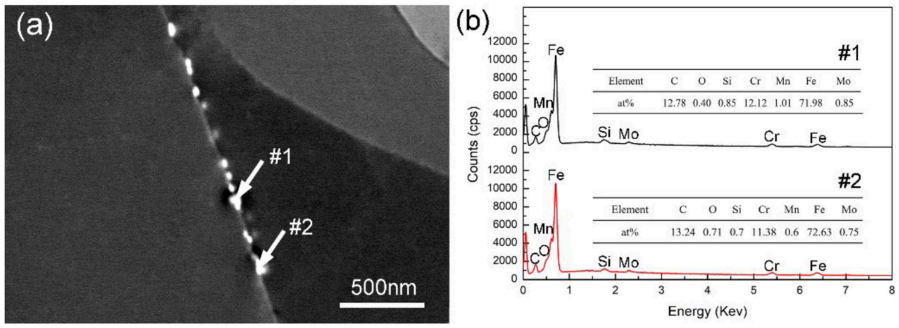

FIGURE 8 | Fine carbide particles precipitate at the grain boundaries in the 12Cr-0.3Y sample: **(a)** BSEI image, **(b)** EDS analysis results.

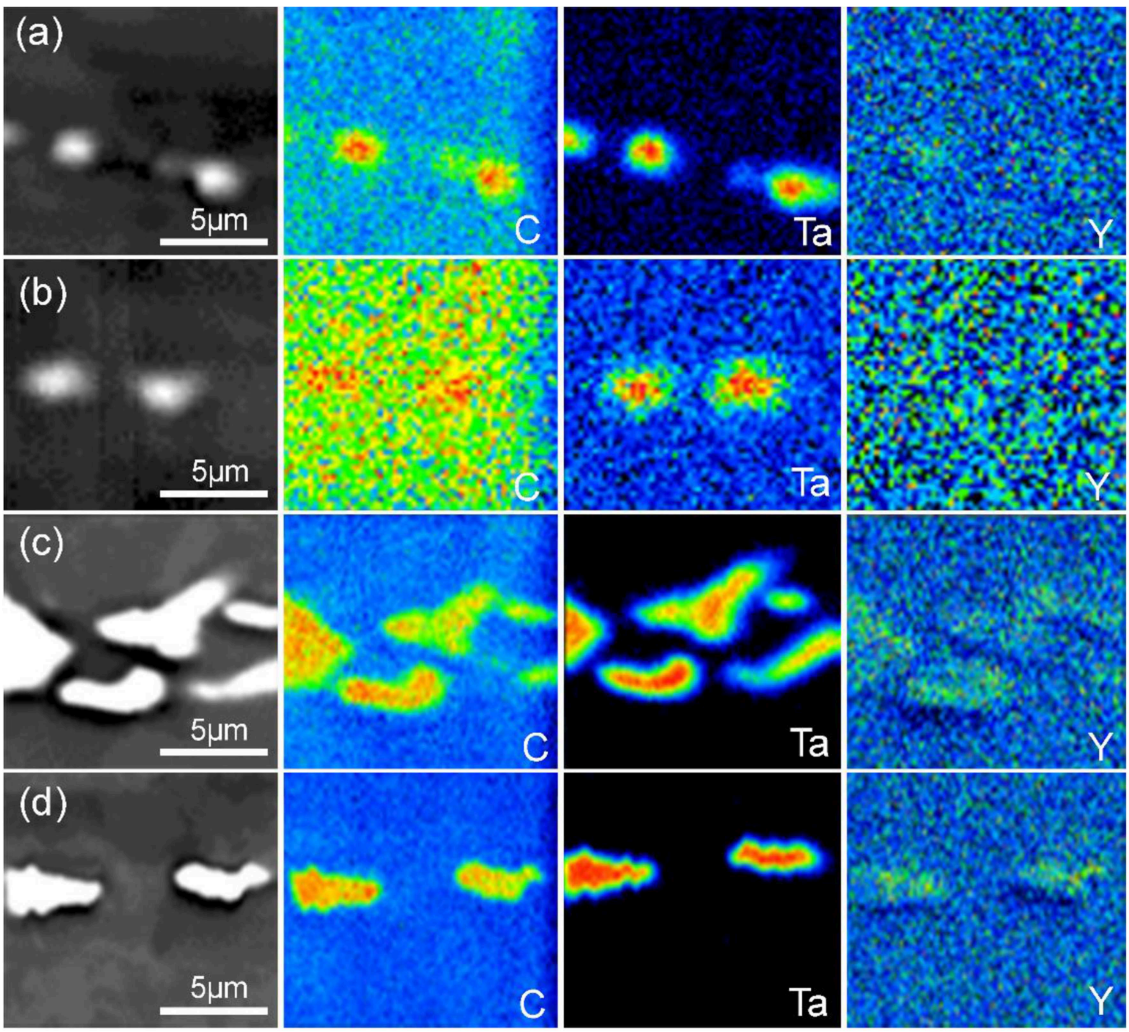

FIGURE 9 | EPMA results showing of particles and element distributions of various samples: **(a)** 12Cr-0Y, **(b)** 12Cr-0.1Y, **(c)** 12Cr-0.2Y, **(d)** 12Cr-0.3Y.

of 20–200 nm. It indicates that the added Ta and Y_2O_3 do not react with C to form the composite oxide or carbide, but only Ta and C react to form TaC carbides and are segregated together with Y_2O_3. Therefore, the particles in the EPMA results (**Figures 10c,d**) are actually a mixture of TaC and Y_2O_3 particles rather than Y-Ta-C composite carbides. It is considered that the interaction of $M_{23}C_6$, TaC, and/or Y_2O_3 with dislocations can not only hinder the movement of dislocations and improve

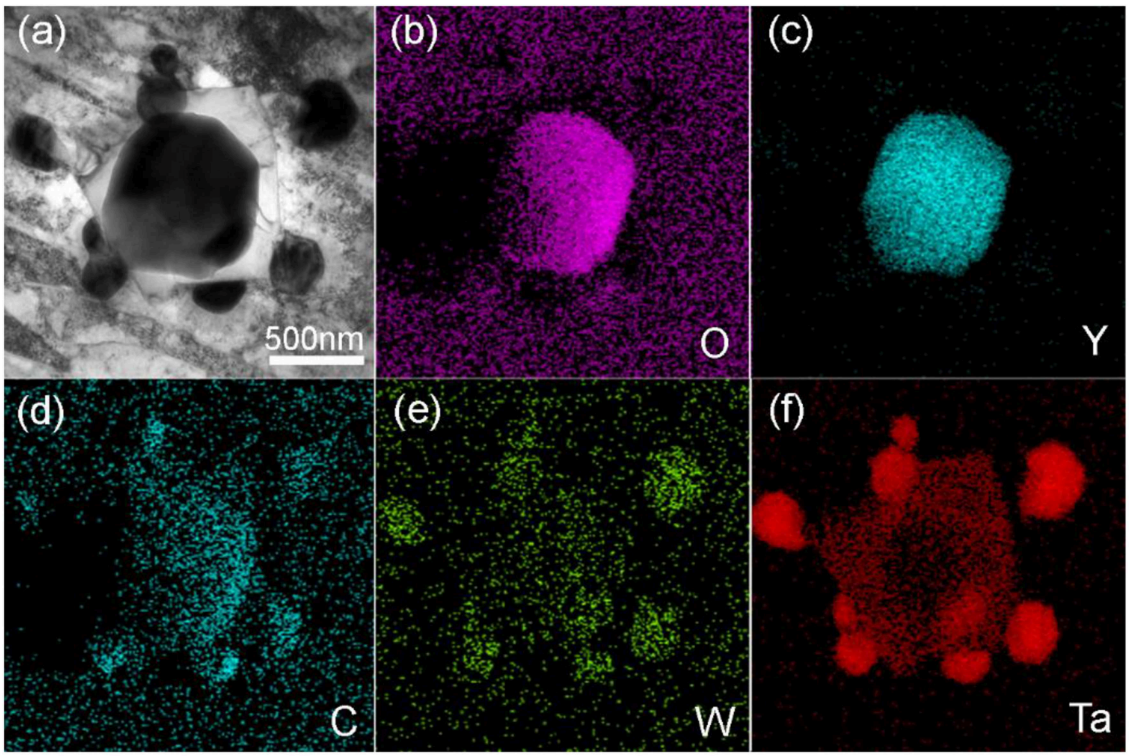

FIGURE 10 | TEM bright field image **(a)** and corresponding EDS maps **(b–f)** showing of Y_2O_3 particle surrounded by fine carbides in the 12Cr-0.3Y sample.

the mechanical properties (Macías-Delgado et al., 2018), but also pin grain boundary migration, thereby improving the high-temperature stability of the ODS steels (Kumar et al., 2017). However, compared with the ODS steel prepared by MA, the size of Y_2O_3 particles introduced by self-oxidation is much larger in this study. For the MA method, the added Y_2O_3 powder is broken and even dissolved and precipitates again in the form of composite oxide particles during the long-term of high-energy ball milling, resulting in a distribution of nano-scale structured Y-M-O (M=Cr, Ti, Si, etc.) particles (Larson et al., 2001; Ukai and Fujiwara, 2002; Miller et al., 2003). In this study, whether cast, forging or hot-rolling, the energy is much lower than that of high-energy ball milling. That is, there is not sufficient energy to break and refine the Y_2O_3 particles. Instead, the original Y_2O_3 particles formed during casting have survived without being dissolved or refined during subsequent hot-forging and hot-rolling. Generally, the nano-sized oxide particles are believed to have a strong strengthening effect on the matrix due to the formation of the Orowan loops (Zhang and Chen, 2006; Wang et al., 2013; Xu et al., 2019). Obviously, the coarse Y_2O_3 particles have little dispersion strengthening effect to the steel matrix compared to the nano-sized Y-M-O particles, but the thermal stability and anti-neutron radiation performance of the Y-M-O particles is not as good as that of the Y_2O_3 particles (Zeybek et al., 2014).

The particle density (number of particles per area) measured Image-J software is shown in **Figure 11**. It should be noted that the statistical particles herein refer to all particles, including the Y_2O_3 oxide and MC carbides. It can be seen that there is no significant change in particle density as the Y content increases. This also indicates that although the Y content of the different samples is different, the particle size of the Y_2O_3 produced by auto-oxidation is relatively large, resulting in no significant difference in particle density between these samples.

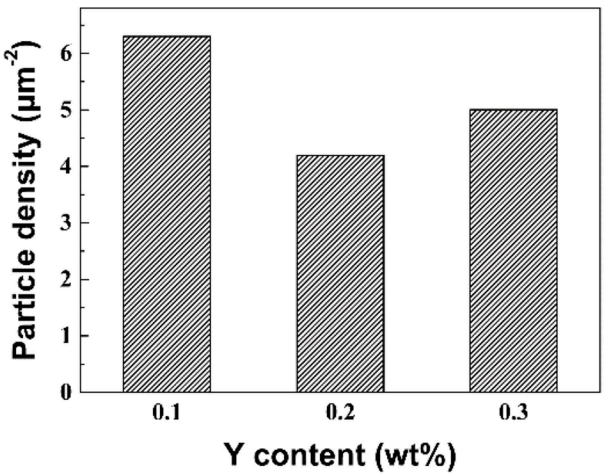

FIGURE 11 | Particle density (number of particles per area) of various samples with different yttrium content.

Scenario 3: Microhardness

Vickers hardness plotted as a function of the Y additions is shown in **Figure 12**. It can be seen that as the amount of

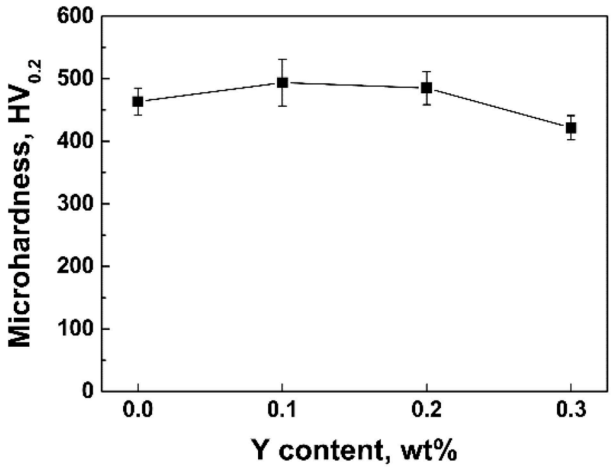

FIGURE 12 | Vickers hardness plotted as a function of the Y additions.

Y added increases, the hardness first increases to 494 HV (12Cr-0.1Y) and then decreases to 422 HV (12Cr-0.3Y). In this study, it is considered that the contribution to the hardness mainly comes from three aspects: composite strengthening of the dual-phase structured matrix, texture strengthening of the matrix, and dispersion strengthening of the second phase particles. As described above, as the Y addition increases, the relative content of martensite phase and the texture densities do not change significantly, so the hardness variation induced by the Y addition is closely related to the change in the second phase strengthening. The hardness of the 12Cr-0.1Y sample is higher than that (463 HV) of the 12Cr-0Y, which may be mainly due to the dispersion strengthening effect of the introduced yttria particle. As discussed above, when the amount of Y addition is increased to 0.3 wt%, the yttria particles tend to aggregate with the $M_{23}C_6$ and TaC particles, resulting in coarsening of the original fine carbides. Obviously, the coarsening of the fine particles causes deterioration of the dispersion strengthening, resulting in a decrease in hardness.

Combining casting and self-oxidation of yttrium instead of MA process can avoid the reaction of yttira with other alloying elements. However, the size of the yttira introduced by self-oxidation is much larger than that of the MA. Moreover, as the yttrium addition is high, the yttira particles are easy to be segregated with the fine carbide particles, resulting in coarsening of the particles and reducing the mechanical properties of the ODS steels. Therefore, how to refine the particle size of yttira introduced by self-oxidation and prevent the agglomeration of yttira and carbide particles is one of the key issues in the future research of this method.

CONCLUSIONS

In this study, the 12Cr ODS steels with different Y additions have been fabricated by casting, hot-forging and subsequent hot-rolling. The microstructure and properties were characterized and investigated. The main conclusions are as follows:

(1) The 12Cr ODS steels with different Y additions consist of alternating coarse fiber grained ferrite and martensite laths. The fiber ferrite grains are composed of equiaxed subgrains containing very few dislocations. The ratio of ferrite to martensite and the density of the LABs both within the martensite and ferrite grains do not change significantly.
(2) In the ferrite regions, the {001} <110> texture is observed in the 12Cr-0Y sample, while no typical rolling textures are found in the 12Cr-0.1Y and 12Cr-0.2Y samples. A strong θ-fiber texture running from {001}<110> to {111}<110> is identified in the 12Cr-0.3Y sample. The difference in texture of the ferrite phase is considered to be related to the difference in contents of Y_2O_3 particles.
(3) The Y_2O_3 particles introduced by self-oxidation during casting are survived without being dissolved or refined after hot-forging and hot-rolling. However, they tend to aggregate with fine $M_{23}C_6$ and TaC carbides.
(4) The hardness of the sample with high Y additions is lower than that of the samples with none or low Y additions, which could be attributed to the fact the yttria and TaC particles are prone to aggregate coarsening when the Y addition is high, resulting in a decrease in dispersion strengthening effect.

DATA AVAILABILITY STATEMENT

All datasets generated for this study are included in the article/supplementary material.

AUTHOR CONTRIBUTIONS

JL and PZ: methodology. CW, JL, JT, and NG: investigation. CW, NG, and JL: writing-original draft preparation. NG and JL: writing-review and editing. PZ and HY: supervision. PZ, JL, NG, and QY: funding acquisition.

FUNDING

This work was supported by the National Major R&D Project (Grant No. 2017YFB0702400) and National Natural Science Foundation of China (Nos. 51501158 and 51801190).

ACKNOWLEDGMENTS

JL was very grateful to Prof. Shilei Li at University of Science and Technology Beijing for his help in the EPMA test.

REFERENCES

Abram, T., and Ion, S. (2008). Generation-IV nuclear power: a review of the state of the science. *Energy Policy* 36, 4323–4330. doi: 10.1016/j.enpol.2008.09.059

Calcagnotto, M., Ponge, D., Demir, E., and Raabe, D. (2010). Orientation gradients and geometrically necessary dislocations in ultrafine grained dual-phase steels studied by 2D and 3D EBSD. *Mat. Sci. Eng. A* 527, 2738–2746. doi: 10.1016/j.msea.2010.01.004

Chen, T., Aydogan, E., Gigax, J. G., Chen, D., Wang, J., Wang, X., et al. (2015). Microstructural changes and void swelling of a 12Cr ODS ferritic-martensitic alloy after high-dpa self-ion irradiation. *J. Nucl. Mater.* 467, 42–49. doi: 10.1016/j.jnucmat.2015.09.016

Chen, Y., Zhang, F., Yan, Q., Zhang, X., and Hong, Z. (2019). Microstructure characteristics of 12Cr ferritic/martensitic steels with various yttrium additions. *J. Rare Earths* 37, 547–554. doi: 10.1016/j.jre.2018.08.013

Corpace, F., Monnier, A., Grall, J., Manaud, J.-P., Lahaye, M., and Poulon-Quintin, A. (2017). Resistance upset welding of ODS steel fuel claddings—evaluation of a process parameter range based on metallurgical observations. *Metals* 7:333. doi: 10.3390/met7090333

Guo, N., Li, D., Yu, H., Xin, R., Zhang, Z., Li, X., et al. (2017). Annealing behavior of gradient structured copper and its effect on mechanical properties. *Mater. Sci. Eng. A* 702, 331–342. doi: 10.1016/j.msea.2017.07.023

Guo, N., Zhang, Z. M., Dong, Q. S., Yu, H. B., Song, B., Chai, L. J., et al. (2018). Strengthening and toughening austenitic steel by introducing gradient martensite via cyclic forward/reverse torsion. *Mater. Des.* 143, 150–159. doi: 10.1016/j.matdes.2018.01.058

Kestens, L., Jonas, J. J., Van Houtte, P., and Aernoudt, E. (1996). Orientation selective recrystallization of nonoriented electrical steels. *Metallur. Mater. Trans. A* 27, 2347–2358. doi: 10.1007/BF02651889

Kestens, L. A. I., and Pirgazi, H. (2016). Texture formation in metal alloys with cubic crystal structures. *Mater. Sci. Technol.* 32, 1303–1315. doi: 10.1080/02670836.2016.1231746

Khaleghi, E., Lin, Y.-S., Meyers, M. A., and Olevsky, E. A. (2010). Spark plasma sintering of tantalum carbide. *Scr. Mater.* 63, 577–580. doi: 10.1016/j.scriptamat.2010.06.006

Kim, B.-R., Woo, K.-D., Doh, J.-M., Yoon, J.-K., and Shon, I.-J. (2009). Mechanical properties and rapid consolidation of binderless nanostructured tantalum carbide. *Ceramics Int.* 35, 3395–3400. doi: 10.1016/j.ceramint.2009.06.012

Kimura, Y., Takaki, S., Suejima, S., Uemori, R., and Tamehiro, H. (1999). Ultra grain refining and decomposition of oxide during super-heavy deformation in oxide dispersion ferritic stainless steel powder. *ISIJ Int.* 39, 176–182. doi: 10.2355/isijinternational.39.176

Klueh, R. L., Gelles, D. S., Jitsukawa, S., Kimura, A., Odette, G. R., Van Der Schaaf, B., et al. (2002a). Ferritic/martensitic steels – overview of recent results. *J. Nucl. Mater.* 307–311, 455–465. doi: 10.1016/S0022-3115(02)01082-6

Klueh, R. L., Maziasz, P. J., Kim, I. S., Heatherly, L., Hoelzer, D. T., Hashimoto, N., et al. (2002b). Tensile and creep properties of an oxide dispersion-strengthened ferritic steel. *J. Nucl. Mater.* 307–311, 773–777. doi: 10.1016/S0022-3115(02)01046-2

Klueh, R. L., Shingledecker, J. P., Swindeman, R. W., and Hoelzer, D. T. (2005). Oxide dispersion-strengthened steels: a comparison of some commercial and experimental alloys. *J. Nucl. Mater.* 341, 103–114. doi: 10.1016/j.jnucmat.2005.01.017

Kumar, D., Prakash, U., Dabhade, V. V., Laha, K., and Sakthivel, T. (2017). High yttria ferritic ODS steels through powder forging. *J. Nucl. Mater.* 488, 75–82. doi: 10.1016/j.jnucmat.2016.12.043

Larson, D. J., Maziasz, P. J., Kim, I. S., and Miyahara, K. (2001). Three-dimensional atom probe observation of nanoscale titanium-oxygen clustering in an oxide-dispersion-strengthened Fe-12Cr-3W-0.4Ti + Y_2O_3 ferritic alloy. *Scripta Mater.* 44, 359–364. doi: 10.1016/S1359-6462(00)00593-5

Li, Y., Huang, Q., Wu, Y., Nagasaka, T., and Muroga, T. (2007). Mechanical properties and microstructures of China low activation martensitic steel compared with JLF-1. *J. Nucl. Mater.* 367–370, 117–121. doi: 10.1016/j.jnucmat.2007.03.012

Lin, H.-P., Chen, Y.-C., Chen, D., and Kuo, J.-C. (2014). Effect of cold deformation on the recrystallization behavior of FePd alloy at the ordering temperature using electron backscatter diffraction. *Mater. Character.* 94, 138–148. doi: 10.1016/j.matchar.2014.05.018

Locatelli, G., Mancini, M., and Todeschini, N. (2013). Generation IV nuclear reactors: current status and future prospects. *Energy Policy* 61, 1503–1520. doi: 10.1016/j.enpol.2013.06.101

Lu, C.-Y., Lu, Z., and Liu, C.-M. (2013). Microstructure of nano-structured ODS CLAM steel by mechanical alloying and hot isostatic pressing. *J. Nucl. Mater.* 442, S148–S152. doi: 10.1016/j.jnucmat.2013.01.297

Macías-Delgado, J., Leguey, T., and De Castro, V. (2018). Effect of hot cross rolling on the microstructure and mechanical properties of an Fe-14Cr ODS ferritic steel. *Mater. Sci. Eng. A* 711, 448–459. doi: 10.1016/j.msea.2017.11.067

Miller, M. K., Kenik, E. A., Russell, K. F., Heatherly, L., Hoelzer, D. T., and Maziasz, P. J. (2003). Atom probe tomography of nanoscale particles in ODS ferritic alloys. *Mater. Sci. Eng. A* 353, 140–145. doi: 10.1016/S0921-5093(02)00680-9

Murty, K. L., and Charit, I. (2008). Structural materials for Gen-IV nuclear reactors: challenges and opportunities. *J. Nucl. Mater.* 383, 189–195. doi: 10.1016/j.jnucmat.2008.08.044

Patricia, B.-G. M., and John, J. J. (1996). Effect of finishing temperature on hot band textures in an IF steel. *ISIJ Int.* 36, 68–73. doi: 10.2355/isijinternational.36.68

Rahmanifard, R., Farhangi, H., and Novinrooz, A. J. (2015). Effect of zirconium and tantalum on the microstructural characteristics of 12YWT ODS steel nanocomposite. *J. Alloys Compounds* 622, 948–952. doi: 10.1016/j.jallcom.2014.11.018

Ren, J., Yu, L., Liu, Y., Liu, C., Li, H., and Wu, J. (2018). Effects of Zr addition on strengthening mechanisms of Al-alloyed high-Cr ODS steels. *Materials* 11:118. doi: 10.3390/ma11010118

Saito, S. (2010). Role of nuclear energy to a future society of shortage of energy resources and global warming. *J. Nucl. Mater.* 398, 1–9. doi: 10.1016/j.jnucmat.2009.10.002

Ukai, S., and Fujiwara, M. (2002). Perspective of ODS alloys application in nuclear environments. *J. Nucl. Mater.* 307–311(Part 1), 749–757. doi: 10.1016/S0022-3115(02)01043-7

Wang, M., Zhou, Z., Sun, H., Hu, H., and Li, S. (2013). Microstructural observation and tensile properties of ODS-304 austenitic steel. *Mater. Sci. Eng. A* 559, 287–292. doi: 10.1016/j.msea.2012.08.099

Xu, S., Zhou, Z., Long, F., Jia, H., Guo, N., Yao, Z., et al. (2019). Combination of back stress strengthening and Orowan strengthening in bimodal structured Fe−9Cr–Al ODS steel with high Al addition. *Mater. Sci. Eng. A* 739, 45–52. doi: 10.1016/j.msea.2018.09.111

Yao, Z., Zhang, K. H., Zhou, Z., Daymond, M. R., Jublot-Leclerc, S., and Kaitasov, O. (2018). *In situ* heavy ion irradiation in ferritic/martensitic ODS steels at 500°C. *Mater. Sci. Technol.* 34, 42–46. doi: 10.1080/02670836.2017.1353660

Zeybek, A., Barroso, S. P., Chong, K. B., Edwards, L., and Fitzpatrick, M. E. (2014). Incorporation of Y_2O_3 particles into 410L stainless steel by a powder metallurgy route. *J. Mater. Eng. Perform.* 23, 2120–2130. doi: 10.1007/s11665-014-0988-6

Zhang, Z., and Chen, D. L. (2006). Consideration of Orowan strengthening effect in particulate-reinforced metal matrix nanocomposites: a model for predicting their yield strength. *Scripta Mater.* 54, 1321–1326. doi: 10.1016/j.scriptamat.2005.12.017

Zhang, Z., Dong, Q., Song, B., He, H., Chai, L., Guo, N., et al. (2019). Effect of shear strain rate on microstructure and properties of austenitic steel processed by cyclic forward/reverse torsion. *Materials* 12:506. doi: 10.3390/ma12030506

Zhao, Q., Ma, Z., Yu, L., Li, H., Wang, Z., and Liu, Y. (2018a). Inhibition effect of Ti on the formation of martensite lath in 14Cr oxide dispersion strengthened steel. *Metals* 8:802. doi: 10.3390/met8100802

Zhao, Q., Yu, L., Ma, Z., Li, H., Wang, Z., and Liu, Y. (2018b). Hot deformation behavior and microstructure evolution of 14Cr ODS steel. *Materials* 11:1044. doi: 10.3390/ma11061044

Zhou, S., Zhou, G., Jiang, S., Fan, P., and Hou, H. (2017). Flexible and refractory tantalum carbide-carbon electrospun nanofibers with high modulus and electric conductivity. *Mater. Lett.* 200, 97–100. doi: 10.1016/j.matlet.2017.04.115

Conflict of Interest: The authors declare that the research was conducted in the absence of any commercial or financial relationships that could be construed as a potential conflict of interest.